

Live imaging of astrocyte responses to acute injury reveals selective juxtavascular proliferation

Sophia Bardehle^{1,2}, Martin Krüger³, Felix Buggenthin^{4,5}, Julia Schwausch², Jovica Ninkovic², Hans Clevers⁶, Hugo J Snippert⁶, Fabian J Theis^{4,5}, Melanie Meyer-Luehmann^{7,8}, Ingo Bechmann³, Leda Dimou^{1,2} & Magdalena Götz^{1,2,9}

Astrocytes are thought to have important roles after brain injury, but their behavior has largely been inferred from postmortem analysis. To examine the mechanisms that recruit astrocytes to sites of injury, we used *in vivo* two-photon laser-scanning microscopy to follow the response of GFP-labeled astrocytes in the adult mouse cerebral cortex over several weeks after acute injury. Live imaging revealed a marked heterogeneity in the reaction of individual astrocytes, with one subset retaining their initial morphology, another directing their processes toward the lesion, and a distinct subset located at juxtavascular sites proliferating. Although no astrocytes actively migrated toward the injury site, selective proliferation of juxtavascular astrocytes was observed after the introduction of a lesion and was still the case, even though the extent was reduced, after astrocyte-specific deletion of the RhoGTPase Cdc42. Thus, astrocyte recruitment after injury relies solely on proliferation in a specific niche.

The diversity of functions proposed for reactive astrocytes after brain injury^{1–5} underlines the inadequacy of our current understanding of astrocyte responses to brain damage. Thus, both beneficial roles, such as restoration of ionic homeostasis in the extracellular milieu, wound healing and limitation of inflammation^{2,5}, and deleterious functions, such as scar formation⁴, have been attributed to astrocyte reactions to brain injury. However, very little is known about how astrocytes perform such functions. Do all astrocytes participate in all of these processes or are some astrocytes specialized for particular tasks, such as limiting the invasion of immune cells, antigen presentation⁶ or scar formation? The answer to this question obviously has a bearing on whether, and how, one can selectively promote beneficial and inhibit adverse functions following brain injury. For example, if a certain subset of astrocytes is involved in scar formation, it might be beneficial to constrain their activity specifically. To form a scar, astrocytes must accumulate around the injury site, and it is thought that astrocytes do so by actively migrating toward the lesion and, under some conditions, proliferating nearby^{5,6}. However, this concept of astrocyte recruitment is largely based on *postmortem* immunohistochemical analyses^{7,8}, as astrocyte migration and dynamic orientation toward an injury site have so far only been studied *in vitro* using the scratch-wound assay^{9,10}. If, when and how astrocyte migration occurs after injury *in vivo*, and to what degree it might contribute to increasing astrocyte numbers around the injury site, have not yet been investigated by live imaging *in vivo*. Similarly, other important aspects of astrocyte behavior in response to injury, such as the extent of cell death or proliferation, can only be assessed by live imaging.

This also holds true for the crucial issue of functional heterogeneity. Protein and gene expression analyses have suggested an element of heterogeneity among astrocytes reacting to injury, with, for example, only subsets upregulating specific intermediate filaments, such as nestin^{3,11} or MHC molecules⁶. However, it is entirely unknown whether such subpopulations are actually committed to specific functions, such as migration or interaction with immune cells, or whether all astrocytes can take on all of these functions over time.

To tackle these questions, it is essential to follow single, identifiable astrocytes by live imaging. We used *in vivo* two-photon laser-scanning microscopy (2pLSM)^{12,13} to visualize and monitor astrocyte reactions over time via an implanted cranial window, following acute traumatic brain injury (TBI) inflicted by localized stabbing of the somatosensory cortex as previously described^{7,10}. Using the progeny (referred to as GLAST/eGFP mice) of crosses between the GLAST^{CreERT2} knock-in mouse line¹⁴ (Cre recombinase is expressed in the endogenous *Glact* (also known as *Slc1a3*) locus) and an inducible enhanced (e)GFP reporter strain¹⁵ allowed us to label protoplasmic astrocytes in the gray matter⁷ with GFP (**Supplementary Movie 1**), and to continuously observe changes in the behavior of GFP⁺ astrocytes for up to 28 d after the time of injury (**Figs. 1 and 2**).

RESULTS

Astrocytes react heterogeneously to TBI

We assessed the morphology of GFP⁺ astrocytes by live 2pLSM during the first imaging session on the day of the operation

¹Physiological Genomics, Institute of Physiology, Ludwig-Maximilians University Munich, Munich, Germany. ²Institute for Stem Cell Research, Helmholtz Zentrum Munich, Neuherberg, Germany. ³Institute of Anatomy, University of Leipzig, Leipzig, Germany. ⁴Institute of Bioinformatics and Systems Biology, Helmholtz Zentrum Munich, Neuherberg, Germany. ⁵Department of Mathematics, Technical University Munich, Germany. ⁶Hubrecht Institute, Koninklijke Nederlandse Akademie van Wetenschappen and University Medical Center Utrecht, Connecticut Utrecht, The Netherlands. ⁷Adolf Butenandt Institute, Department of Biochemistry, Ludwig-Maximilians University Munich, Munich, Germany. ⁸Neurocenter, Department of Neurology, University of Freiburg, Freiburg, Germany. ⁹Munich Cluster for Systems Neurology (SyNergy), Munich, Germany. Correspondence should be addressed to M.G. (magdalena.goetz@helmholtz-muenchen.de).

Received 11 October 2012; accepted 27 February 2013; published online 31 March 2013; doi:10.1038/nn.3371

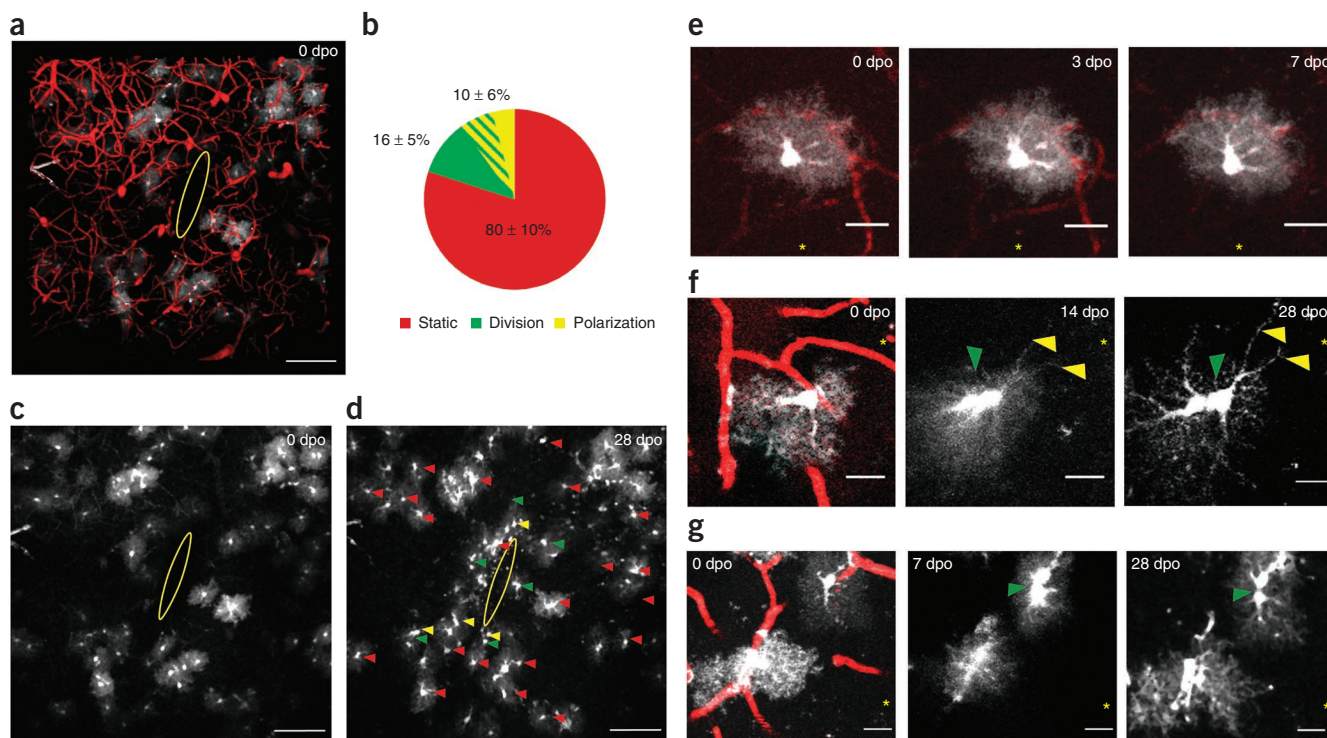


Figure 1 Live imaging of astrocyte responses to a punctate lesion. **(a)** GFP-labeled astrocytes (white) in the vicinity of a punctate lesion (yellow ellipse) in the somatosensory cortex of GLAST/eGFP mice, imaged live by 2pLSM at 0 dpo. Blood vessels are labeled with Texas Red–dextran, and the image shows a three-dimensional view of a 200- μ m-deep *x-y-z* stack. **(b)** Astrocyte behavior was classified into three categories on the basis of the morphological changes observed by 7 d after wounding: cells retained a stable morphology (static), became polarized and/or underwent division ($n = 5$ mice, mean \pm s.e.m.). **(c–g)** Repeated observations of the same cells within 300 μ m of the lesion from 0 dpo **(c)** up to 28 dpo **(d)**; 200- μ m-deep *z* projection) revealed a markedly heterogeneous reaction: the majority of cells retained a stable morphology **(d)**, red arrowheads; an example is shown in **e**, and only a few cells became polarized toward the injury site **(d)**, yellow arrowheads; example in **f** and/or underwent cell division **(d)**, green arrowheads; examples in **f,g**. The yellow asterisks in **e–g** indicate the lesion site. Scale bars represent 100 μ m **(a,c,d)** and 20 μ m **(e–g)**.

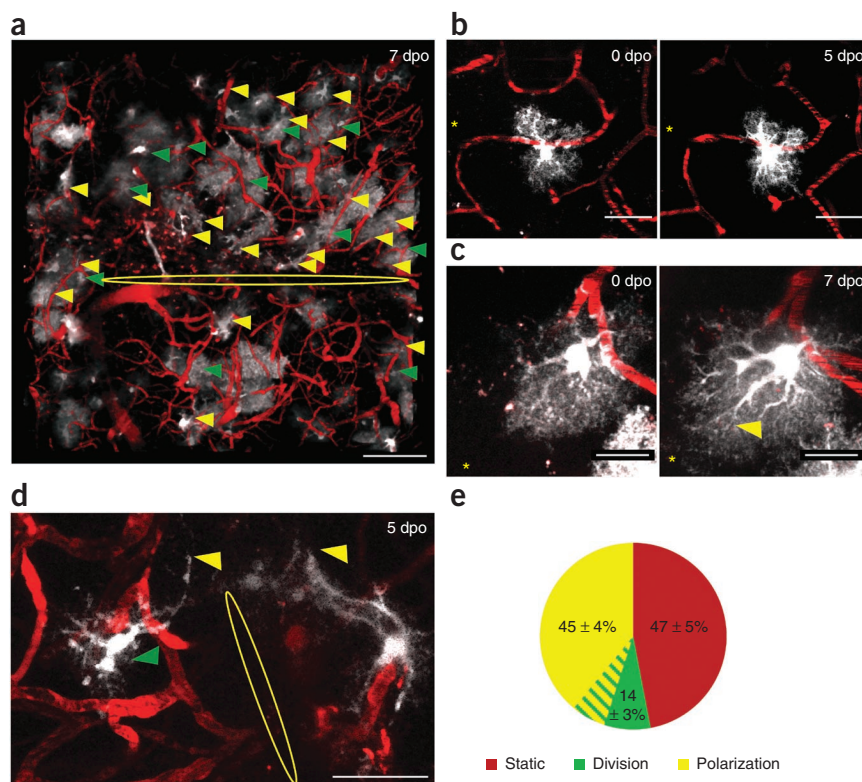
(0 d post-operation (dpo), typically 30 min after injury). At this time, all GFP⁺ cells exhibited the round and bushy morphology typical of protoplasmic astrocytes (Fig. 1a,c,e–g). We inflicted relatively small ‘punctate’ lesions (200 μ m long and 800 μ m deep) on GLAST/eGFP mice (the lesion size was defined as the cell-free area that was devoid of blood vessels labeled with Texas Red–conjugated dextran; Fig. 1a). Virtually all astrocytes could be reliably identified during the course of the entire experiment, and little or no cell death was observed. Most astrocytes (80% of 102 cells from 5 mice) maintained their morphology for up to 4 weeks after wounding (static; Fig. 1b,d,e), in spite of the fact that GFAP was upregulated in virtually all of the astrocytes close to the injury site, as revealed by immunohistochemical analysis at 7 d after injury (Supplementary Fig. 1).

We were unable to detect any migration of astrocytes toward punctate wounds, even after close examination using blood vessels as stable landmarks. To detect even small cell movements, we precisely superimposed images of the same cells acquired at different time points, after correction for tissue contraction. This confirmed that astrocyte positions remained stable and provided no evidence for cell migration (Supplementary Fig. 2). However, we did observe signs of hypertrophy, polarization or proliferation of astrocytes, as previously described *in vitro*^{9,10,16}. In about half of all astrocytes (42%), the soma was enlarged and cell processes were thicker at 7 dpo than at 0 dpo, indicating that the cells had entered a hypertrophic state (Supplementary Fig. 3d). Some cells (10%) formed elongated processes (defined as at least threefold longer than the radius of the cell) that were directed toward the lesion site (polarization; Fig. 1b,d,f). Such changes were not observed after cranial window

insertion without prior injury of the cortex (Supplementary Fig. 4). We also observed astrocytes that had divided (16%; Fig. 1b), typically at 5–7 dpo (Fig. 1d,f,g). Each of these proliferating astrocytes generated no more than two daughter cells, which remained close together for the entire time of observation, even up to 4 weeks (Fig. 1f,g). Most cell divisions were found within 100 μ m of the injury (Supplementary Fig. 5b), and polarization preceded 38% of all cell divisions (Fig. 1b,f), that is, the majority of the cells that proliferated were not polarized, but divided as round bushy astrocytes (Fig. 1g). Notably, the somata of most dividing astrocytes were located directly adjacent to a blood vessel (Fig. 1f,g, and Supplementary Movies 2 and 3), whereas others made contact with vessels by means of extended processes (Fig. 1e). This difference cannot be accounted for by differences in the local density of blood vessels, as only a minority of the astrocytes (33%, see below) were in direct contact with the vasculature via their cell somata. Such cells have been referred to as perivascular astrocytes^{17,18}.

To determine whether these astrocytes may be particularly prone to resume proliferation after more extensive injury, we made incisions (stab wounds) of about 1 mm long and 800 μ m deep before insertion of the cranial window (Fig. 2a). This type of injury activated astrocytes over a wider area, as almost all of the astrocytes within 300 μ m of the injury site upregulated GFAP (*postmortem* analysis; Supplementary Fig. 6). Moreover, in this case, a greater fraction of astrocytes than in mice with punctate wounds (86% \pm 7%) became hypertrophic (Fig. 2b and Supplementary Fig. 3a,d), as revealed by a marked increase in the mean volume of cell somata (Supplementary Fig. 3b). These values are based on direct comparison of measurements for 12 individual cells

Figure 2 Live imaging of astrocyte responses to a stab wound. **(a)** Heterogeneous reaction of GFP⁺ astrocytes within 300 μm of a large stab wound (yellow ellipse) was observed live at 7 dpo by 2pLSM (the image shows a three-dimensional view of a 450- μm -deep x - y - z stack) using Texas Red–dextran to label blood vessels. **(b)** Example of a cell that became hypertrophic, but essentially retained its initial morphology and maintained its position. These cells with static position and no polarization or proliferation were the largest population, as depicted in the pie chart in **e**. **(c,d)** Examples of cells that polarized toward the lesion (yellow arrowheads in **a**, **c** and **d**) and/or showed cell divisions that were identifiable as newly appearing cell duplets at 5 dpo (green arrowheads in **a** and **d**). **(e)** The pie chart summarizes the behavior of astrocytes within 300 μm of the stab wound, as assessed on the basis of morphological changes occurring between 0 and 7 dpo ($n = 3$ mice, mean \pm s.e.m.). Scale bars represent 100 μm (**a**), 50 μm (**b,d**) and 20 μm (**c**). The lesion site is marked by the yellow ellipse (**a,d**) or with yellow asterisks (**b,c**).



from three mice imaged at the indicated times, which yielded a mean volume ratio of 3 ± 0.4 , whereas control cells maintained their initial volume (**Supplementary Fig. 3c**). Thus, after more extensive injury, the somata of virtually all astrocytes increased in size (**Fig. 2b** and **Supplementary Fig. 3a,d**), although this was not necessarily associated with a change in overall morphology (**Fig. 2b**).

Moreover, a subset of astrocytes (45%) within 300 μm of a large stab wound became polarized. Polarization typically occurred within

3–5 dpo (**Fig. 2c–e** and **Supplementary Movie 4**), with processes extending up to 111 μm (mean \pm s.e.m., $69 \pm 5 \mu\text{m}$, $n = 3$ mice), that is, more than threefold longer than the average radius of protoplasmic astrocytes at 0 dpo ($\leq 30 \mu\text{m}$, $25 \pm 0.5 \mu\text{m}$, $n = 3$ mice). Notably, none of the astrocytes, not even the polarized ones, exhibited any detectable signs of movement toward the injury site ($\leq 5 \mu\text{m}$ over 7 d; **Supplementary Fig. 2** and **Supplementary Movie 5**). Just as in the case of the smaller punctate wound, only a subset of astrocytes in the region of the larger stab wound divided within 7 dpo (14%; **Fig. 2a,d,e**), and never generated more than two daughter cells. However, the induction of astrocyte proliferation was no longer restricted to the immediate vicinity ($<100 \mu\text{m}$) of the injury, but occurred over a larger area around the stab wound (**Supplementary Fig. 5**). Again, the vast majority of astrocyte divisions observed by live imaging after a stab wound (71%, $n = 8$ cells) occurred in cells whose somata were directly apposed to a blood vessel (**Fig. 3a–c**).

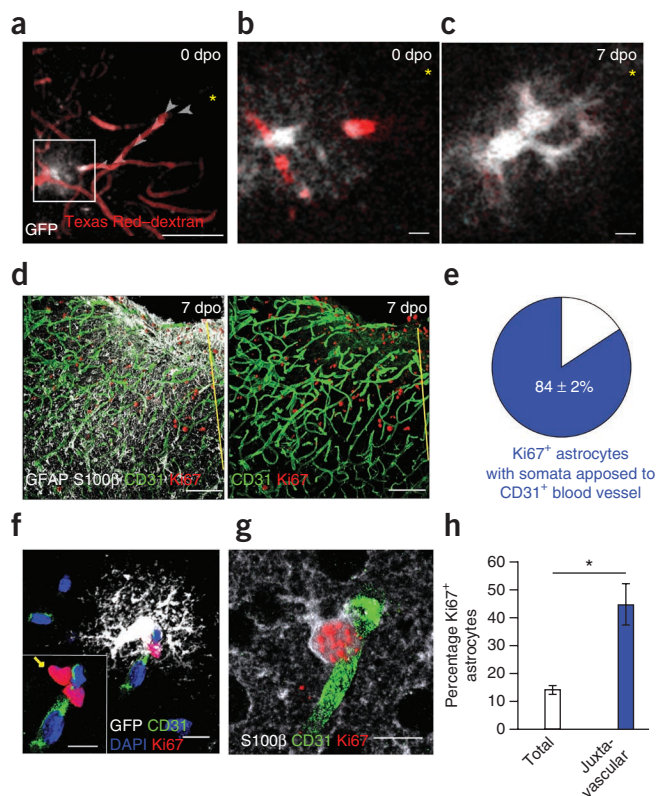
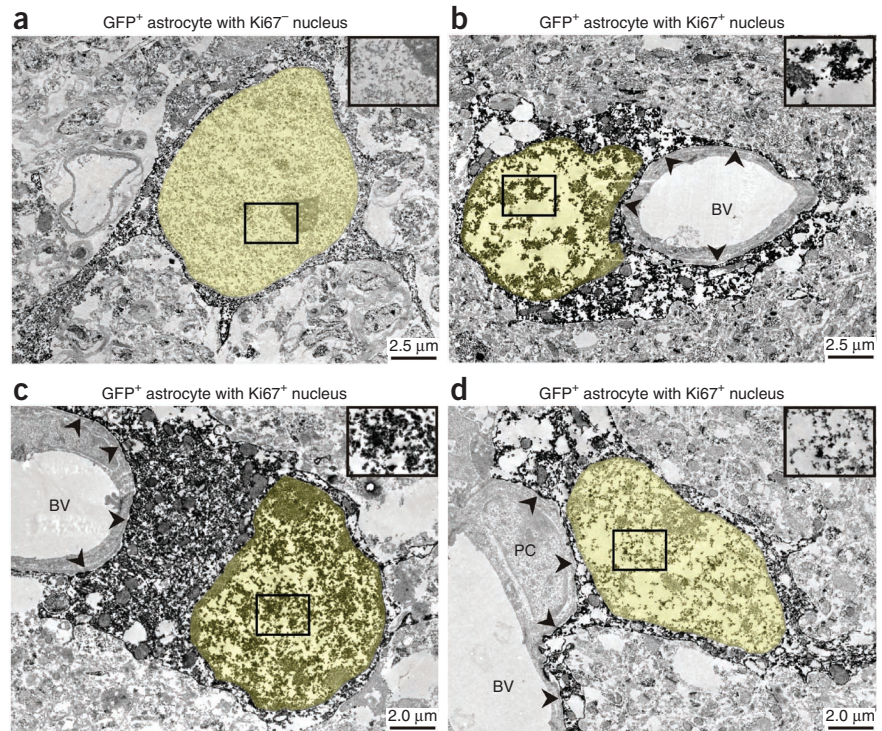


Figure 3 Astrocyte proliferation adjacent to blood vessels. **(a,b)** Live imaging of a GFP⁺ astrocyte 30 min after localized wounding on 0 dpo (close-up in **b**, see **Supplementary Movie 2**) revealed direct contact between the cell soma and a blood vessel (0 dpo, arrowheads). **(c)** The same cell imaged 7 d later (7 dpo) showed up as a cell duplet, indicating that the astrocyte had undergone cell division in close proximity to the vasculature (**Supplementary Movie 3**). The yellow asterisks in **a–c** indicate the lesion site.

(d–h) Quantitative analysis by immunolabeling confirmed proliferation (Ki67⁺ nuclei) of astrocytes, which were labeled with GFAP and S100 β (**d,g**) or with GFP (**f**), close to CD31⁺ endothelial cells of cerebral blood vessels 7 d after infliction of a stab wound. **(e)** The majority of astrocytes with Ki67⁺ nuclei were in direct contact with blood vessels (mean \pm s.e.m.); examples are shown for juxtavascular proliferating astrocytes labeled with GFP (**f**) or S100 β (**g**) from GLAST/eGFP mice. The yellow arrow in the insert of **f** indicates the Ki67⁺ nucleus of the GFP⁺ cell shown in white in **f**. **(h)** Astrocytes that were directly apposed to blood vessels showed a higher proliferation rate than the total astrocyte population (mean \pm s.e.m., unpaired t test, $*P = 0.040$). Scale bars represent 100 μm (**a,d**) and 20 μm (**b,c,f,g**).

Figure 4 Juxtavascular locations of proliferating astrocytes. (a–d) Immunoelectron microscopy of GFP⁺ astrocytes from *Aldh1l1-eGFP* mice after stab wounding (7 dpo), identified by double-labeling for GFP⁺ and Ki67-DAB, confirmed proliferation of astrocytes in direct contact with cerebral blood vessels (BVs). Positive DAB labeling resulted in the expected granular staining pattern visible in the cytoplasm of GFP⁺ astrocytes, as well as in Ki67⁺ nuclei of proliferating cells (b–d). Although most parenchymal astrocytes (a) did not proliferate, a proliferating subset of GFP⁺ Ki67⁺ astrocytes was found preferentially in juxtavascular locations, where cell somata made direct contacts with the fused glio-vascular basement membrane (marked with arrowheads in b–d) at brain capillaries and post-capillary vessels. The nuclei of astrocytes are shaded in yellow. Insets show close-ups of boxed regions in the respective nuclei, with typical DAB grains indicative of Ki67 immunoreactivity (b–d), whereas the nucleus in a is Ki67⁻. PC, pericyte.



Taken together, our *in vivo* imaging data reveal a marked lack of migration of reactive astrocytes, as well as a notable heterogeneity of response, with subsets of astrocytes polarizing toward the injury site, and a rather specific subset of astrocytes with their soma in direct contact with the vasculature showing a particular tendency to proliferate.

Preferentially juxtavascular astrocytes proliferate

To examine the locations of proliferating astrocytes independently of GLAST^{CreERT2}-mediated recombination, we used immunostaining to detect actively proliferating (Ki67⁺) cells (mostly microglia and NG2 glia⁸) that were astrocytes (S100β⁺ and/or GFAP⁺) and with their soma in direct vicinity to endothelial cells (CD31⁺) lining the blood vessels (Fig. 3d). Although only 33% of all astrocytes (1,049 cells, 3 mice) were located with their somata directly adjacent to CD31⁺ endothelial cells, 84% of all proliferating (Ki67⁺) astrocytes (194 cells, 5 mice; Fig. 3e) were found to display such direct apposition to a blood vessel (Fig. 3f,g). Indeed, among astrocytes whose somata were in direct contact with a blood vessel, the fraction that proliferated

within 7 d of stab wounding was threefold higher (45%) than in the astrocyte population as a whole (14%; Fig. 3h), further supporting the concept that astrocytes in this position are more prone to divide than others.

However, direct apposition, as defined at the light microscopic level, may well overlook intervening cells or even misinterpret the position of cells in relation to the different basement membranes surrounding the blood vessels¹⁹. To clarify the exact location of dividing astrocytes, we used pre-embedding immunoelectron microscopy to determine the location of dividing (Ki67⁺) astrocytes labeled by GFP in *Aldh1l1-eGFP* mice^{20,21} 7 d after stab wounding. GFP⁺ cells with or without Ki67 labeling were localized in vibratome sections (Supplementary Fig. 7) and further processed for electron microscopy (Fig. 4). Although many Ki67-negative astrocytes were found in the parenchyma (Fig. 4a), the somata of Ki67⁺ GFP⁺ astrocytes were

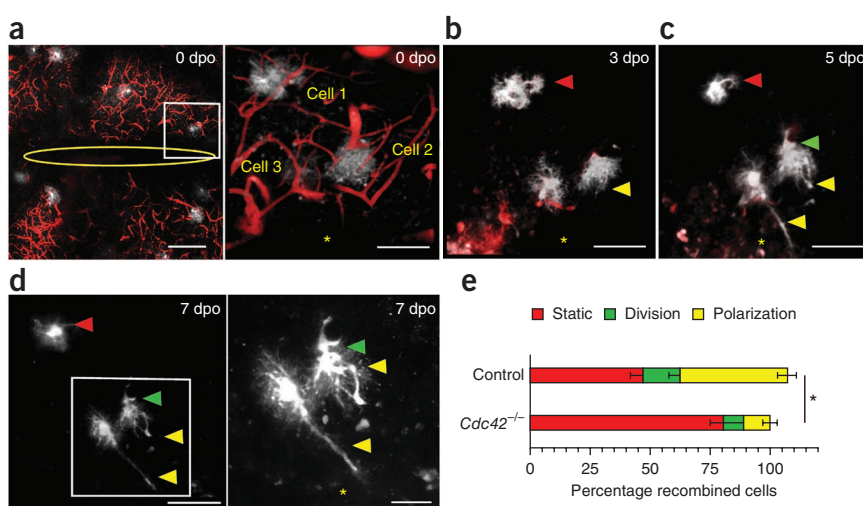


Figure 5 Live imaging of *Cdc42*^{-/-} astrocytes following stab wounding. (a–d) The behavior of *Cdc42*^{-/-} astrocytes labeled with GFP was observed live by 2pLSM in GLAST/eGFP *Cdc42*^{loxP/loxP} mice after stab wounding. A heterogeneous reaction of astrocytes following injury was also detected in *Cdc42*^{-/-} astrocytes. Although many cells retained a static morphology (cell 1, a; red arrowhead, b–d), a few cells polarized toward the lesion site (cells 2 and 3, a; yellow arrowheads, b–d) or underwent division (green arrowhead, c,d). Boxed regions in a,d are enlarged in right panels. Scale bars represent 100 μm (a, left), 50 μm (a, right; b,c; d, left) and 25 μm (d, right). (e) Compared with control mice with normal *Cdc42* expression, fewer *Cdc42*^{-/-} astrocytes in the vicinity of a stab wound exhibited morphological changes or showed signs of polarization, implying that the ability of these astroglia to respond to injury was impaired ($n = 3$ mice per group, mean \pm s.e.m., one-way ANOVA, $*P = 0.0373$). The lesion site is marked with yellow asterisks.

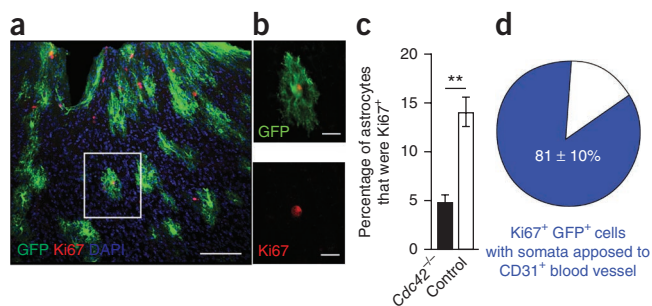


Figure 6 Proliferation defect in *Cdc42*^{-/-} astrocytes following injury. (a–c) Immunolabeling of astrocytes in GLAST/eGFP *Cdc42*^{loxP/loxP} mice revealed a significant decrease in the numbers of proliferating (Ki67⁺ nuclei) *Cdc42*^{-/-} GFP⁺ astrocytes observed after stab wounding (7 dpo, higher magnification of boxed region shown in **b**) compared with the proliferation rate of control astrocyte with normal *Cdc42* expression (mean \pm s.e.m., unpaired *t* test, $**P = 0.001$). (d) Most of the proliferating *Cdc42*^{-/-} astrocytes were located in direct contact with a blood vessel (mean \pm s.e.m.). Scale bars represent 100 μ m (**a**) and 25 μ m (**b**).

always closely associated with blood vessels (**Fig. 4b–d**). In many cases, the Ki67⁺ nucleus was only separated by a small astrocytoplasmic bridge from the neighboring blood vessel, and no other cells or processes could be detected between the soma of the Ki67⁺ astrocyte and the fused glio-vascular basement membrane surrounding the vessels (**Fig. 4b–d**). Most proliferating astrocytes ($n = 14$ cells) were found at capillaries or postcapillary vessels that were anatomically defined, for example, by their diameter, the presence of smooth muscle cells and basement membrane architecture¹⁹. Some astrocytes were located in close proximity to pericytes (**Fig. 4d**), but were always separated from these by the fused glio-vascular basement membrane, thereby clearly determining their position as juxtavascular, rather than perivascular¹⁹. As no additional basement membrane was detected on the parenchymal side of Ki67⁺ GFP⁺ astrocytes, a putative location in the perivascular (Virchow-Robin) space could always be ruled out, and their position was, by definition, juxtavascular, that is, inside the brain parenchyma proper (**Supplementary Fig. 8**).

Astrocyte proliferation occurs clonally

Live observations of astrocyte duplets suggested that each pair represented the daughter cells derived from the division of a single mother cell. Given that virtually no cell migration was observed, it seems highly unlikely that a different cell could have adventitiously moved into apposition with a previously identified cell in the interval between two successive imaging sessions. Nevertheless, we wished to confirm the clonal nature of astrocyte duplets directly, using an independent technique. To this end, we crossed GLAST^{CreERT2} mice with the multi-color *R26R-Confetti* reporter strain²² (referred to as GLAST/Confetti mice), which allows for inducible labeling of astrocytes with one of four different fluorescent proteins, membrane-bound cyan fluorescent protein, nuclear GFP, or cytoplasmic yellow or red fluorescent protein. To perform a clonal analysis on the progeny of reactive astrocytes, we treated adult mice with low doses of tamoxifen, which induced sparse labeling of less than 25 astrocytes of each color per hemisphere of the cerebral cortex (**Supplementary Fig. 9**). Although no astrocyte duplets were detected in control, non-lesioned brains or in the contralateral hemisphere of clonally induced GLAST/Confetti mice subjected to unilateral stab wounding, cell duplets of each of the four colors were found in the ipsilateral, lesioned hemisphere, and were always unicolored (defined as pairs of cell somata of the same color $\leq 5 \mu$ m apart, 20 sections from 3 animals). Given that all astrocyte

duplets ($n = 18$ duplets in 2 brains at 7 dpo; **Supplementary Fig. 9b–e**) appeared close to the injury site ($<500 \mu$ m away) and were always of a single color, we concluded that each duplet was the product of a single cell division.

The absence of any larger clusters of cells of the same color confirms the observation, based on repeated imaging of live cells, that a given astrocyte undergoes no more than a single division over the course of our experiments, although the possibility of a further division rapidly followed by cell death cannot formally be excluded. With regard to the extent of astrocyte expansion after injury, both live imaging and clonal labeling revealed that the increase in astrocyte numbers was limited. Only a minority of astrocytes divides at all, each generating just two daughter cells, and no cells migrated into the area adjacent to the wound.

Effect of *Cdc42* deletion on astrocyte reactions to injury

However, even small changes in the number of astrocytes can have substantial effects on microglia activation¹⁰ or leukocyte immigration⁵. We set out to explore the role of a candidate molecule that might participate in regulating the proliferation of juxtavascular astrocytes, the population responsible for increasing astrocyte numbers after stab wounding. The small RhoGTPase *Cdc42* is a major signaling mediator that is involved in many proliferative pathways^{23,24} and has been implicated in astrocyte recruitment by polarized cell migration *in vitro*^{9,10}. Thus, deletion of the *Cdc42* gene in astrocytes allowed us to further test for possible changes in cell position or the formation of processes.

To investigate the intrinsic role of *Cdc42* in astrocyte reactions to injury, we monitored GFP-labeled astrocytes lacking *Cdc42* by live imaging in tamoxifen-induced GLAST/eGFP *Cdc42*^{loxP/loxP} mice¹⁰ after inflicting a stab wound injury about 1 mm in length (**Fig. 5**). Live observation by 2pLSM revealed that the number of *Cdc42*^{-/-} astrocytes that extended elongated processes toward the injury site was markedly lower than that observed in GLAST/eGFP *Cdc42*^{+/+} controls (*Cdc42*^{-/-}, 11%; *Cdc42*^{+/+}, 45%; three mice per genotype; **Fig. 5**). The incidence of cell division among *Cdc42*^{-/-} astrocytes was likewise reduced (*Cdc42*^{-/-}, 8.5%; *Cdc42*^{+/+}, 14%; **Fig. 5c–e**), and those cells that did divide were restricted to within 100 μ m of the injury. In control mice, dividing astrocytes were found up to 300 μ m from the site of the wound.

Immunohistochemical analysis of similarly lesioned GLAST/eGFP *Cdc42*^{loxP/loxP} mice confirmed the proliferation defect in *Cdc42*^{-/-} astrocytes (**Fig. 6a–c**). Only 5% of *Cdc42*^{-/-} astrocytes (1,031 cells, $n = 5$ mice; **Fig. 6c**) are actively dividing (Ki67⁺ nuclei) at 7 dpo, compared with 14% of astrocytes (1,049 cells, $n = 3$ mice; **Fig. 6c**) in control mice with normal *Cdc42* expression. Although deletion of *Cdc42* in astrocytes impaired the frequency of polarization and proliferation, the proliferating subset of astrocytes was still found preferentially in juxtavascular positions (81%, $n = 6$ mice; **Fig. 6d**). Thus, even when proliferation of the juxtavascular subset is impaired, astrocytes located at other sites apparently do not compensate for that. This is compatible with the notion that the population of reactive astrocytes is made up of distinct subsets dedicated to specific tasks, such as proliferation or polarization.

DISCUSSION

The ability to repeatedly examine the same small area of tissue *in vivo* using live imaging can provide new insights into the detailed pathology of diverse CNS disorders, including Alzheimer's disease²⁵, multiple sclerosis²⁶ and axonal degeneration in the spinal cord^{27–29}. We used this technique to monitor the reaction of astroglia to TBI

and discovered a marked degree of heterogeneity in astrocyte behavior. Although most astrocytes became hypertrophic and upregulated GFAP after stab wounding (**Supplementary Figs. 1, 3 and 6**), only subsets of them polarized or proliferated. In stark contrast with data obtained *in vitro* with scratch wound assays^{9,10,16}, our *in vivo* observations revealed that most astrocytes in the lesioned region, including those that polarized toward the injury site or proliferate, stayed in their initial positions after TBI. Thus, not only do astrocytes remain in their region of developmental origin, for example, in the cerebral cortex³⁰, and expand in number by proliferation during postnatal stages³¹, they do not even migrate for short distances over periods from days to weeks after TBI, at least not in the gray matter of the cerebral cortex.

Technical considerations

Before considering these observations further, it is important to rule out possible technical artifacts. Clearly, inducible genetic recombination does not allow one to label all astrocytes, but rather provides the opportunity to adjust the density of GFP-labeled astrocytes to levels that are optimal for imaging purposes. Thus, although most astrocytes express GLAST (and 60–80% of all astrocytes coexpress the Cre recombinase from the GLAST locus¹⁴), a subset of astrocytes with lower levels of GLAST expression³² will not be labeled by inducible genetic recombination. To rule out the possibility that our observations reported are applicable only to the subset of astrocytes with higher levels of GLAST (and thus CreERT2), we performed three sets of control experiments: live imaging after stab wounding of *Aldh1l1-eGFP* mice, in which the entire astrocyte population is labeled^{20,21} (**Supplementary Fig. 10a–e** and **Supplementary Movie 6**), live imaging in *GFAP-eGFP* mice³³, in which the astrocytes with the highest GFAP expression levels are labeled (**Supplementary Fig. 10f–h**), and immunostaining to verify the results obtained in the above-mentioned transgenic lines. Live imaging of the control mouse lines confirmed the immobility of most astrocytes, as no cell migration was observed in these strains either. Furthermore, we confirmed the juxtavascular location of proliferating astrocytes by live imaging and immunostaining in both of the transgenic mouse lines. Thus, our results were confirmed in three independent mouse lines and can reasonably be applied to the entire astrocyte population. In this regard, the behavior of GLAST/eGFP-labeled astrocytes may be viewed as representative of that of astrocytes in general.

We were also able to rule out several technical concerns in regard to our 2pLSM imaging technique, as we were able to clearly visualize the migration of other glial populations, such as NG2 glia, toward injury sites (A. von Streitberg, C. Straube, M.G. & L.D., unpublished data), consistent with previous observations of microglial cells^{13,34}. Thus, most glial cells readily migrated to injury sites in the gray matter of the cerebral cortex after stab wound injury, whereas astrocytes failed to do so. It will be interesting to examine whether this also holds true for white matter regions or other injury conditions, and whether astrocytes generally do not migrate in the mammalian brain *in vivo*.

Astrocyte recruitment to injury sites

Our findings that astrocytes did not migrate have marked implications for the mechanism of recruitment to sites of injury, as they imply that astrocyte numbers increase after TBI solely as a result of proliferation. Notably, the increase in astrocyte numbers after such stab wound injury is relatively modest (about 20%), which is consistent with the limited amount of proliferation that we observed. In this context, it is important to stress that the increase observed by GFAP immunostaining in many pathological samples does not reflect an increase

in astrocyte numbers, but rather upregulation of GFAP expression. In many, if not most, brain regions, astrocytes are GFAP negative under normal, healthy conditions, as is the case in the gray matter of the cerebral cortex^{33,35}. Thus, the enormous increase in GFAP⁺ cells may give a misleading impression, considering that total astrocyte numbers showed only a modest increase.

The astrocytes that proliferated and generated two daughter cells, which remained close together, were mainly found at juxtavascular locations. Astrocytes whose somata lie directly adjacent to blood vessels have been described previously in the retina¹⁸ and somatosensory cortex in mouse¹⁷, and have been referred to as perivascular astrocytes. On the basis of our electron microscopic data, which localized the somata of proliferating astrocytes in regard to the glio-vascular basement membrane in the juxtavascular parenchyma rather than to a perivascular (Virchow-Robin) space (enclosed between two basement membranes), we refer to these as the juxtavascular subset of astrocytes given the earlier localization of pericytes¹⁹ and microglia^{26,36}. It will now be important to determine whether this population is widespread in the CNS or has a more restricted, possibly even region-specific, distribution.

These data raise the question of the functional relevance of this class of astrocytes. When proliferating astrocytes were selectively ablated by expression of herpes simplex virus thymidine kinase (HSV-TK) under the control of the *Gfap* promoter, leukocyte infiltration was markedly enhanced³⁷, prompting the suggestion that juxtavascular astrocytes, and their expansion after injury, may be important for limiting invasion of these cells into the brain. As recent data also imply that pericyte-derived cells contribute to fibrotic scar formation³⁸, it is tempting to speculate that juxtavascular astrocytes may also limit migration and/or proliferation of these cells. Thus, this juxtavascular subset of astrocytes is in a privileged position to interact with cells invading injured brain areas^{26,38,39}. Taken together, our live-imaging data, which reveal that a rather special type of astrocytes is the major contributor to proliferation after TBI, prompts new ideas about the role of astrocytes in this specific location. Likewise, one may have to reconsider the issue of a direct contribution of astrocytes to scar formation, given their limited increase in number and failure to migrate to the actual injury site. However, it will certainly be of interest to apply this analysis to other injury models, such as stroke or selective inflammatory lesions, to observe astrocyte behavior under these different conditions, given that their patterns of gene expression also differ markedly⁶.

Astrocyte heterogeneity

Irrespective of the exact function of the juxtavascular astrocytes, our observation of a specific subset of astrocytes proliferating after stab wound injury reveals a notable functional heterogeneity in astrocyte behavior. This heterogeneity also extends further, as we observed a distinct subset of astrocytes that polarized toward the lesion site, whereas others retained their bushy morphology despite clearly reacting to injury by becoming hypertrophic. As we were able to follow reactive astrocytes for days and weeks after injury, we could verify that subsets of astrocytes retained their bushy morphology at all times after injury, rather than extending long polarized processes and retracting them again.

Astrocytes that did polarize typically extended their elongated processes toward the injury site between 3 and 5 d after stab wounding, and maintained them for several weeks, as has been described in epilepsy models⁴⁰. Notably, the proportion of astrocytes that proliferated did not increase as a function of the injury size, although a higher proportion of astrocytes polarized toward a larger injury.

This further supports the idea that at least three different sets of astrocytes react in distinct ways to stab wound injury. This is important because it provides a basis for selective regulation of the different subsets of astrocytes, not only to unravel their specific functions, but eventually to modulate these functions with a view to improving outcomes after brain injury. Our data therefore not only revise the current view of astrocyte recruitment to injury^{2,5}, but also highlight the heterogeneity of astrocyte behavior, which suggests a division of labor in response to local lesions, and provide the basis for new approaches to ameliorating functional deficits following injury.

METHODS

Methods and any associated references are available in the [online version of the paper](#).

Note: Supplementary information is available in the [online version of the paper](#).

ACKNOWLEDGMENTS

We are indebted to C. Brakebusch for the *Cdc42^{loxP/loxP}* mice, S. Robel for initial help in setting up the two-photon live-imaging procedure, and C. Straube and S. Falkner for sharing their imaging expertise. We would also like to thank R. Wabner, C. Meyer, D. Franzen, I. Mühlhahn and G. Jäger for technical assistance, and M. Hübener, D.E. Bergles, J. McCarter and P. Hardy for critical comments on the manuscript. We thank the DFG (German Research foundation) whose support (particularly via the Leibniz Prize and SFB 870) allowed us to invest into this new experimental area and for funding M.G. and F.J.T. by SPP1356 and I.B. by DFG-FOR 1336. In addition, this work was supported by the BMBF (Ministry of Science and Education) to M.G. and F.J.T., the Helmholtz Association (Helmholtz Alliance ICEMED to M.G., I.B. and F.J.T.; Helmholtz Alliance on Systems Biology to M.G. and F.J.T.), the Emmy Noether Program of the DFG (ME 3542/1-1 to M.M.-L.), the European Research Council (starting grant 'LatentCauses' to F.J.T.) and Munich Cluster for Systems Neurology. The Initial Training Network Edu-GLIA (PITN-GA-2009-237956) funded by the European Commission under the Seventh Framework Program (FP7) provided a wonderful discussion platform for glial research.

AUTHOR CONTRIBUTIONS

S.B. performed all of the experiments and data analyses (except for electron microscopy) and wrote the manuscript. M.K. and I.B. carried out electron microscopy. F.B. and F.J.T. assisted in data processing and volume analysis (Supplementary Figs. 2 and 3). J.S., J.N., H.C. and H.J.S. supplied the GLAST/cfetti mouse strain (Supplementary Fig. 9). M.M.-L. provided access to the 2pLSM and expert advice on imaging. L.D. initially established the *in vivo* two-photon microscopy technique and taught it to S.B. M.G., together with L.D., designed the project and experiments, discussed the results and wrote the manuscript. M.G. coordinated and directed the project.

COMPETING FINANCIAL INTERESTS

The authors declare no competing financial interests.

Reprints and permissions information is available online at <http://www.nature.com/reprints/index.html>.

- Hellal, F. *et al.* Microtubule stabilization reduces scarring and causes axon regeneration after spinal cord injury. *Science* **331**, 928–931 (2011).
- Pekny, M. & Nilsson, M. Astrocyte activation and reactive gliosis. *Glia* **50**, 427–434 (2005).
- Robel, S., Berninger, B. & Götz, M. The stem cell potential of glia: lessons from reactive gliosis. *Nat. Rev. Neurosci.* **12**, 88–104 (2011).
- Silver, J. & Miller, J.H. Regeneration beyond the glial scar. *Nat. Rev. Neurosci.* **5**, 146–156 (2004).
- Sofroniew, M.V. Molecular dissection of reactive astrogliosis and glial scar formation. *Trends Neurosci.* **32**, 638–647 (2009).
- Zamanian, J.L. *et al.* Genomic analysis of reactive astrogliosis. *J. Neurosci.* **32**, 6391–6410 (2012).
- Buffo, A. *et al.* Origin and progeny of reactive gliosis: a source of multipotent cells in the injured brain. *Proc. Natl. Acad. Sci. USA* **105**, 3581–3586 (2008).
- Simon, C., Götz, M. & Dimou, L. Progenitors in the adult cerebral cortex: cell cycle properties and regulation by physiological stimuli and injury. *Glia* **59**, 869–881 (2011).
- Etienne-Manneville, S. *In vitro* assay of primary astrocyte migration as a tool to study Rho GTPase function in cell polarization. *Methods Enzymol.* **406**, 565–578 (2006).
- Robel, S., Bardehle, S., Lepier, A., Brakebusch, C. & Götz, M. Genetic deletion of *Cdc42* reveals a crucial role for astrocyte recruitment to the injury site *in vitro* and *in vivo*. *J. Neurosci.* **31**, 12471–12482 (2011).
- Sirko, S. *et al.* Reactive glia in the injured brain acquire stem cell properties in response to Sonic hedgehog. *Cell Stem Cell* (in the press) (2013).
- Holtmaat, A. *et al.* Long-term, high-resolution imaging in the mouse neocortex through a chronic cranial window. *Nat. Protoc.* **4**, 1128–1144 (2009).
- Nimmerjahn, A., Kirchhoff, F. & Helmchen, F. Resting microglial cells are highly dynamic surveillants of brain parenchyma *in vivo*. *Science* **308**, 1314–1318 (2005).
- Mori, T. *et al.* Inducible gene deletion in astroglia and radial glia—a valuable tool for functional and lineage analysis. *Glia* **54**, 21–34 (2006).
- Nakamura, T., Colbert, M.C. & Robbins, J. Neural crest cells retain multipotential characteristics in the developing valves and label the cardiac conduction system. *Circ. Res.* **98**, 1547–1554 (2006).
- Höltje, M. *et al.* Role of Rho GTPase in astrocyte morphology and migratory response during *in vitro* wound healing. *J. Neurochem.* **95**, 1237–1248 (2005).
- McCaslin, A.F., Chen, B.R., Radosevich, A.J., Cauli, B. & Hillman, E.M. *In vivo* 3D morphology of astrocyte-vasculature interactions in the somatosensory cortex: implications for neurovascular coupling. *J. Cereb. Blood Flow Metab.* **31**, 795–806 (2011).
- Reichenbach, A. & Wolburg, H. Astrocytes and ependymal glia. in *Neuroglia*, 2nd edn. (Kettenmann, H. & Ransom, B.R.) 19–35 (Oxford University Press, 2005).
- Krueger, M. & Bechmann, I. CNS pericytes: concepts, misconceptions and a way out. *Glia* **58**, 1–10 (2010).
- Cahoy, J.D. *et al.* A transcriptome database for astrocytes, neurons and oligodendrocytes: a new resource for understanding brain development and function. *J. Neurosci.* **28**, 264–278 (2008).
- Heintz, N. Gene expression nervous system atlas (GENSAT). *Nat. Neurosci.* **7**, 483 (2004).
- Snippert, H.J. *et al.* Intestinal crypt homeostasis results from neutral competition between symmetrically dividing Lgr5 stem cells. *Cell* **143**, 134–144 (2010).
- Fuchs, S. *et al.* Stage-specific control of neural crest stem cell proliferation by the small rho GTPases *Cdc42* and *Rac1*. *Cell Stem Cell* **4**, 236–247 (2009).
- Warner, S.J., Yashiro, H. & Longmore, G.D. The *Cdc42/Par6/aPKC* polarity complex regulates apoptosis-induced compensatory proliferation in epithelia. *Curr. Biol.* **20**, 677–686 (2010).
- Meyer-Luehmann, M. *et al.* Rapid appearance and local toxicity of amyloid-beta plaques in a mouse model of Alzheimer's disease. *Nature* **451**, 720–724 (2008).
- Davalos, D. *et al.* Fibrinogen-induced perivascular microglial clustering is required for the development of axonal damage in neuroinflammation. *Nat. Commun.* **3**, 1227 (2012).
- Ertürk, A. *et al.* Three-dimensional imaging of the unsectioned adult spinal cord to assess axon regeneration and glial responses after injury. *Nat. Med.* **18**, 166–171 (2012).
- Misgeld, T., Nikic, I. & Kerschensteiner, M. *In vivo* imaging of single axons in the mouse spinal cord. *Nat. Protoc.* **2**, 263–268 (2007).
- Dibaj, P. *et al.* *In vivo* imaging reveals rapid morphological reactions of astrocytes towards focal lesions in an ALS mouse model. *Neurosci. Lett.* **497**, 148–151 (2011).
- Tsai, H.H. *et al.* Regional astrocyte allocation regulates CNS synaptogenesis and repair. *Science* **337**, 358–362 (2012).
- Ge, W.P., Miyawaki, A., Gage, F.H., Jan, Y.N. & Jan, L.Y. Local generation of glia is a major astrocyte source in postnatal cortex. *Nature* **484**, 376–380 (2012).
- Regan, M.R. *et al.* Variations in promoter activity reveal a differential expression and physiology of glutamate transporters by glia in the developing and mature CNS. *J. Neurosci.* **27**, 6607–6619 (2007).
- Nolte, C. *et al.* GFAP promoter-controlled EGFP-expressing transgenic mice: a tool to visualize astrocytes and astrogliosis in living brain tissue. *Glia* **33**, 72–86 (2001).
- Fuhrmann, M. *et al.* Microglial *Cx3cr1* knockout prevents neuron loss in a mouse model of Alzheimer's disease. *Nat. Neurosci.* **13**, 411–413 (2010).
- Middeldorp, J. & Hol, E.M. GFAP in health and disease. *Prog. Neurobiol.* **93**, 421–443 (2011).
- Mathiesen, T.M., Lehre, K.P., Danbolt, N.C. & Ottersen, O.P. The perivascular astroglial sheath provides a complete covering of the brain microvessels: an electron microscopic 3D reconstruction. *Glia* **58**, 1094–1103 (2010).
- Bush, T.G. *et al.* Leukocyte infiltration, neuronal degeneration, and neurite outgrowth after ablation of scar-forming, reactive astrocytes in adult transgenic mice. *Neuron* **23**, 297–308 (1999).
- Göriz, C. *et al.* A pericyte origin of spinal cord scar tissue. *Science* **333**, 238–242 (2011).
- Prodinger, C. *et al.* CD11c-expressing cells reside in the juxtavascular parenchyma and extend processes into the glia limitans of the mouse nervous system. *Acta Neuropathol.* **121**, 445–458 (2011).
- Oberheim, N.A. *et al.* Loss of astrocytic domain organization in the epileptic brain. *J. Neurosci.* **28**, 3264–3276 (2008).

ONLINE METHODS

Mice, tamoxifen treatment and surgical procedures. Adult (2–3 month old) male mice obtained from crosses between GLAST^{CreERT2} and either CAG-CAT-eGFP (GLAST/eGFP)^{14,15}, *Cdc42^{loxP/loxP}* (ref. 41), *R26R-Confetti* reporter mice (GLAST/Confetti)²² or *Aldh1l1-eGFP* mice^{20,21} were used. Tamoxifen was administered by adding it to food (400 mg per kg, LasVendi) in the case of GLAST/eGFP mice. To induce low rates of recombination, GLAST/Confetti mice received a single intraperitoneal injection of 80 µg of tamoxifen per gram of body weight (stock solution: 40 mg ml⁻¹ tamoxifen in corn oil with 10% ethanol) 1 week before surgery.

For repeated imaging, a cranial window was prepared as described previously¹² using tamoxifen-induced GLAST/eGFP and GLAST/eGFP *Cdc42^{loxP/loxP}* mice. In brief, mice were anesthetized with an intraperitoneal injection of midazolam (5 mg per kg of body weight), medetomidine (0.5 mg per kg) and fentanyl (0.05 mg per kg), and a unilateral craniotomy (diameter of 3 mm) was positioned between cranial sutures bregma and lambda above the somatosensory cortex. Punctate wounds were inflicted by inserting a lancet-shaped knife into the cortex to a depth of 0.8 mm; to produce stab lesions, the lancet was moved 1 mm in a lateral direction. The craniotomy was covered with a permanent glass cover slip (5-mm diameter) and sealed with dental acrylic (Paladur, Heraeus). Anesthesia was antagonized with an intraperitoneal injection of atipamezol (2.5 mg per kg), flumazenil (0.5 mg per kg) and naloxone (1.2 mg per kg).

For immunohistochemical analysis of GLAST/eGFP and GLAST/Confetti mice, 2–3-month-old mice were subjected to stab wounds no sooner than 1 week after the last tamoxifen dose. GLAST/eGFP *Cdc42^{loxP/loxP}* mice were analyzed 3 weeks after induction of recombination to ensure clearance of endogenous Cdc42 protein.

All animal experiments were performed in accordance with the Guidelines on the Use of Animals and Humans in Neuroscience Research, revised and approved by the Society of Neuroscience, and licensed by the State of Upper Bavaria.

2pLSM. Anesthetized mice were injected intravenously (tail vein) with 50 µl of a solution (10 mg ml⁻¹) of Texas Red–conjugated dextran (70 kDa; Molecular Probes D1864) to label blood vessels. Head-bar fixed, anesthetized and craniotomized mice were placed on a heated stage, and imaging was performed with an Olympus FV1000MPE microscope equipped with a multi-photon, near-infrared, pulsed MaiTai HP DeepSee laser (Spectra Physics) equipped with a water immersion objective (20× 1.0 NA), an FV10-MRG filter (barrier filter = 495–540 nm, dichromatic mirror = 570 nm, BA 575–630 nm) and internal photomultiplier tube detectors. Emission of intrinsic eGFP signal (astrocytes in green channel) and Texas Red–conjugated dextran (vasculature in red channel) was simultaneously scanned using an excitation wavelength of 910 nm (depth-adjusted laser power <50 mW). Optical sections with a resolution of 512 × 512 pixels in the x-y dimension were acquired at z increments of 5 µm to a depth of maximally 500 µm below the dura. Labeled blood vessels served as landmarks for repetitive imaging of z stacks obtained for the same field of view. The low density of GFP-labeled astrocytes, which was controlled by adjusting the tamoxifen dose, enabled reliable identification and continuous tracing of single cells selected at 0 dpo (first imaging time point 30 min after injury), and these cells were repeatedly monitored at various intervals thereafter (3, 5, 7, 14, 21 or 28 dpo). A maximum of five imaging sessions was performed per mouse. All imaging experiments were performed without detectable phototoxic side effects.

Immunohistochemistry. Mice were anesthetized and transcardially perfused with 4% paraformaldehyde (PFA, vol/vol) in phosphate-buffered saline (PBS) for 20 min. Brains were post-fixed in 4% PFA for 1 h after dissection. Staining of vibratome sections (60 µm thick) was performed as described previously¹⁰ using chick antibody to GFP (1:500, Aves Lab, GFP-1020), mouse antibody to GFAP (1:500, Sigma, G3893), mouse antibody to S100β (1:500, Sigma, S2532), rabbit antibody to Ki67 (1:100, Thermo Fisher Clone, SP6 RM-9106-S), rat antibody to CD31 (1:500, BD, 550274) and rabbit antibody to red fluorescent protein (1:500, Rockland, 600-401-379) as primary antibodies, and fluorophore-coupled (1:500) antibody to chick Alexa488 (Invitrogen, A11039) and antibody to mouse Alexa488 (Invitrogen, A11029) or Cy3 (Dianova 115-165-003), antibody to rabbit Cy3 (Dianova, 711-165-152) and antibody to rat A647 (Invitrogen, A-21247) as secondary antibodies. Nuclei were stained with DAPI (1:10,000, Sigma, D9564) for 5 min at 20–25 °C.

Slides were analyzed with a Zeiss LSM710 confocal laser-scanning microscope using water-immersion objectives (25× 0.8 NA and 40× 1.1 NA).

Data processing and image registration. For visualization and analysis of 2pLSM data, Olympus FV10-ASW 2.0 and ImageJ 1.45q software was used. Cell migration was analyzed using labeled blood vessels as landmarks to bring three-dimensional images of the same area imaged at different time points into register with each other. The color channels of image stacks obtained at different time points were split into four separate grayscale image stacks showing astrocytes and blood vessels at 0 dpo and later time points. Channel splitting and merging was performed with ImageJ⁴². Rigid three-dimensional registration was performed on blood vessel images with elastix 4.5, using day 0 as the fixed and the second time point as the shifted image (Supplementary Fig. 2a)⁴³. This step resolved linear shifts in x, y and z directions, as well as rotations. Next, transformed images were brought into register using an elastic b-spline method^{44,45} to correct for tissue deformation. The calculated transformation parameters were then applied to the stack of images from the GFP channel for the second time point, as well as to a control grid (Supplementary Fig. 2a). Areas of the image that revealed no change relative to the control grid indicated that registration was unreliable because of the lack of blood vessel labeling. Such regions were not used for evaluation of astrocyte migration. Channel splitting and the two-step registration procedure made it possible to precisely overlay different three-dimensional image stacks on the basis of the landmark information provided by the blood vessels. Analysis of superimposed, registered four-color stacks never detected any cell body displacements in images acquired at different time points (Supplementary Fig. 2b–m).

To validate the visual evaluation of cellular hypertrophy, we used a semi-automatic image processing pipeline to measure the volume of individual GFP-labeled cell somata ($n = 12$ hypertrophic cells from three mice, $n = 11$ control cells from four mice) at two different time points based on three-dimensional live-imaging data (Supplementary Fig. 3). For each image stack, optical sections were smoothed with a two-dimensional Gaussian filter (sigma = 0.5) to remove noise. Cell somata were identified by manual three-dimensional thresholding using the ImageJ plug-in 3d object counter v2.0 (ref. 46). The high variability in GFP intensities, influenced by tissue depth, wound reaction, laser power and optical window quality, made it necessary to manually adjust thresholds for each individual cell in three-dimensional z stacks to reliably determine the size of cell somata. The volume (in µm³) of each segmented soma was computed by multiplying the sum of segmented voxels by the calibration in x, y and z direction. Volume ratios were calculated for cell pairs ($n > 10$) by dividing the value for the later time point (5 or 7 dpo) by the value at 0 dpo. A cell was defined as hypertrophic if the volume of the soma increased by more than 10% in the period after injury. All hypertrophic cells used in this analysis displayed volume ratios >1.5.

Immunoelectron microscopy. For electron microscopy, mice were killed and transcardially perfused using a fixative containing 0.1% glutaraldehyde (vol/vol) and 4% PFA. The tissue was post-fixed in the fixative for 4 h. After that, mouse brains were cut into consecutive 60-µm sections on a vibratome (Leica Microsystems) in cooled PBS. After thorough rinsing, unspecific binding of the antibodies was blocked by incubation in PBS containing 5% goat serum (vol/vol). Chick antibody to GFP (1:200, Aves Lab, GFP-1020) and rabbit antibody to Ki67 (1:200 dilution, Thermo Fisher Clone, SP6 RM-9106-S) primary antibodies were incubated overnight at 4 °C. Following thorough rinsing, the appropriate biotinylated secondary antibodies (1:250, Dianova; antibody to rabbit, 111-065-003; antibody to chick, 103-065-155) were incubated with the tissue for 2 h at 20–25 °C. The sections were then rinsed again, and bound antibodies were visualized with the DAB reaction, using a staining kit (Vector Laboratories) according to the manufacturer's protocol. Omission of primary antibodies resulted in the absence of specific staining. Vibratome sections were further processed and embedded in Durcupan (Sigma Aldrich) as described previously³⁹. To restrict the ultrastructural analysis precisely to areas of the stab wound, the lesion site was identified by light microscopy and the blocks of resin were trimmed down to the respective region before ultra-thin sectioning so as to ensure that ultra-thin sections encompassed the lesion site only. Sections (60 nm thick) were prepared on an ultramicrotome (Leica Microsystems), transferred to formvar-coated grids and stained with lead citrate for 6 min. Ultrastructural analysis was performed using a Zeiss SIGMA electron microscope equipped with a STEM detector and Atlas software (Zeiss NTS).

Quantification and statistical analyses. Immunohistochemical analysis was done on multi-channel, confocal three-dimensional stacks, using Zeiss ZEN 2010 software and the Cell Counter plug-in for ImageJ 1.45q. Quantifications on fixed sections were done on 3–6 mice (≥ 3 sections each) per group. The sample size was justified by significance testing and experience from previous immunohistochemical analyses. Results are represented as means \pm s.e.m. calculated between different mice. The single-cell analyses are based on live imaging of a total number of 102 cells from five mice with punctate wounds, 68 cells from three mice with stab wounds, and 25 cells from three *Cdc42*^{-/-} mice with stab wounds. Statistics was performed with GraphPad Prism 4.0. For statistical analysis, data were first tested for their distribution and, if normally distributed, the unpaired, two-tailed Student's *t* test was used; otherwise nonparametric, one-way ANOVA was used for comparing mean values that were considered significantly different.

41. Wu, X. *et al.* Cdc42 controls progenitor cell differentiation and beta-catenin turnover in skin. *Genes Dev.* **20**, 571–585 (2006).
42. Abramoff, M.D., Magalhães, P.J. & Ram, S.J. Image processing with ImageJ. *Biophotonics Int.* **11**, 36–42 (2004).
43. Klein, S., Staring, M., Murphy, K., Viergever, M.A. & Pluim, J.P. elastix: a toolbox for intensity-based medical image registration. *IEEE Trans. Med. Imaging* **29**, 196–205 (2010).
44. Klein, S., Staring, M. & Pluim, J.P. Evaluation of optimization methods for nonrigid medical image registration using mutual information and B-splines. *IEEE Trans. Image Process.* **16**, 2879–2890 (2007).
45. Metz, C.T., Klein, S., Schaap, M., van Walsum, T. & Niessen, W.J. Nonrigid registration of dynamic medical imaging data using nD + t B-splines and a groupwise optimization approach. *Med. Image Anal.* **15**, 238–249 (2011).
46. Bolte, S. & Cordelières, F.P. A guided tour into subcellular colocalization analysis in light microscopy. *J. Microsc.* **224**, 213–232 (2006).

